

## Band structure of a HgTe-based three-dimensional topological insulator

J. Gospodarič<sup>1,\*</sup>, V. Dziom,<sup>1</sup> A. Shuvaev<sup>1</sup>, A. A. Dobretsova<sup>2</sup>, N. N. Mikhailov,<sup>2</sup> Z. D. Kvon,<sup>2</sup> E. G. Novik<sup>3,4</sup> and A. Pimenov<sup>1</sup>

<sup>1</sup>*Institute of Solid State Physics, Vienna University of Technology, 1040 Vienna, Austria*

<sup>2</sup>*Rzhanov Institute of Semiconductor Physics and Novosibirsk State University, Novosibirsk 630090, Russia*

<sup>3</sup>*Dresden High Magnetic Field Laboratory (HLD-EMFL), Helmholtz-Zentrum Dresden-Rossendorf, 01328 Dresden, Germany*

<sup>4</sup>*Institute of Theoretical Physics, Technische Universität Dresden, 01062 Dresden, Germany*



(Received 6 December 2019; revised 5 August 2020; accepted 14 August 2020; published 8 September 2020)

From the analysis of the cyclotron resonance, we experimentally obtain the band structure of the three-dimensional topological insulator based on a HgTe thin film. Top gating was used to shift the Fermi level in the film, allowing us to detect separate resonance modes corresponding to the surface states at two opposite film interfaces, the bulk conduction band, and the valence band. The experimental band structure agrees reasonably well with the predictions of the  $\mathbf{k} \cdot \mathbf{p}$  model. Due to the strong hybridization of the surface and bulk bands, the dispersion of the surface states is close to parabolic in the broad range of the electron energies.

DOI: [10.1103/PhysRevB.102.115113](https://doi.org/10.1103/PhysRevB.102.115113)

### I. INTRODUCTION

The electronic band structure provides an important fingerprint of a material in the reciprocal space. In case the surface of the sample is accessible experimentally, the standard technique of angle-resolved photoemission spectroscopy [1] is an established way to obtain the necessary information. However, in several cases, especially in two-dimensional heterostructures, several buffer or capping layers prevent collecting the data from the photoemitted electrons. As possible alternative methods, the analysis of the cyclotron mass [2–5] or density of states via capacitance experiments [6,7] have been suggested to recover the band dispersion especially of two-dimensional materials. In magneto-optical experiments [8–12], the relevant information is obtained comparing the theoretical predictions [13,14] of the band structure with experimental data.

Within another approach, the band structure may be obtained from the analysis of the cyclotron resonance frequencies [5,15] that is especially useful for two-dimensional materials. Indeed, in two dimensions and in the quasiclassical approximation, the cyclotron frequency  $\Omega_c$  may be written in terms of the cyclotron effective mass  $m_c$  as [16]

$$m_c \equiv \frac{eB}{\Omega_c} = \frac{\hbar^2}{2\pi} \frac{\partial A}{\partial E} \Big|_{E=E_F}. \quad (1)$$

Here,  $B$  is the external magnetic field,  $A$  is the area in the reciprocal space enclosed by the contour of the constant energy  $E$ , and  $E_F$  is the Fermi energy.

An important point is that the cyclotron frequency in Eq. (1) linearly depends on an external magnetic field independently of the form of dispersion relations because the Fermi area is field independent in the quasiclassical approximation. This approximation is the main assumption

in the present experiments [5,15], i.e., transitions between several Landau levels should take place simultaneously. This condition is certainly realized at lower magnetic fields utilized in the present experiment.

In the general case, the relation between the area and the band structure may be complicated. In such cases, an additional input from the theory is indispensable. As discussed in Sec. III, especially for surface states and for bulk conduction band, the isotropic approximation can be applied leading to a simple relation between the Fermi-vector  $k_F$  and the Fermi area:  $A = \pi k_F^2$ . In this case, Eq. (1) can be rewritten as

$$\frac{\partial E}{\partial k} \Big|_{E=E_F} = \frac{\hbar^2 k_F}{m_c}, \quad (2)$$

and, thus, can be directly integrated to obtain the experimental band-structure  $E(k)$ . For the holelike states, however, the isotropic approximation breaks down, and additional information from the theory is necessary to obtain the band structure. A possible approach, in this case, is presented in Sec. III.

In this paper, we apply the procedure sketched above to a three-dimensional topological insulator (3D TI) HgTe and compare the results with the predictions of the  $\mathbf{k} \cdot \mathbf{p}$  model.

The unstrained single-crystalline mercury telluride (HgTe) is a gapless semimetal with the conduction and valence bands formed by  $\Gamma_8$  bands [13]. If grown in the form of a thin film on a CdTe layer, HgTe is subject to a tensile strain due to lattice mismatch between HgTe and CdTe [17]. As a consequence, the originally degenerate light and heavy  $\Gamma_8$  hole bands split at the  $\Gamma$  point, thus, forming a bulk insulator with a gap around  $\sim 20$  meV [17,18] for an 80-nm HgTe film. Due to a band inversion between HgTe and CdTe the topologically protected surface states arise in about 10–20-nm-thick layer close to the boundary. HgTe films, thus, form a strong 3D TI [19]. According to band-structure calculations, the conduction band of an 80-nm HgTe 3D TI is nonparabolical, and it is quantized

\*jan.gospodaric@tuwien.ac.at

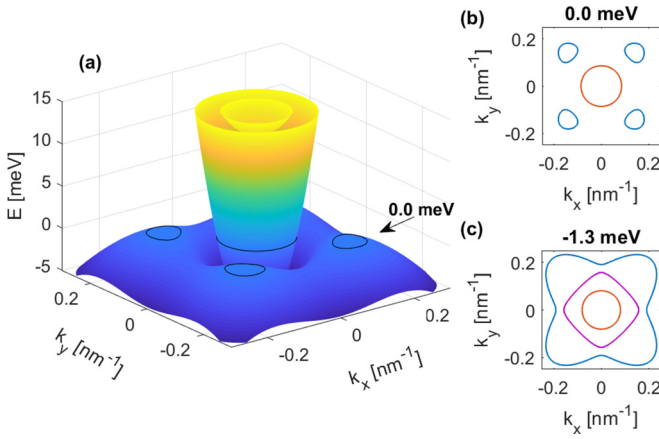


FIG. 1. Theoretical band structure of a 3D topological insulator HgTe. (a) The first valence band, the surface band, and the first conduction band of the 80-nm-thick HgTe layer at the charge neutrality point  $n_{\text{tot}} = 0$  where the concentrations of electrons and holes equal  $\pm 1.2 \times 10^{11} \text{ cm}^{-2}$ . (b) Cross section of (a) at  $E_f = 0 \text{ meV}$ . Blue: holelike Fermi surface ( $\partial A/\partial E < 0$ ) from the islands in the  $(\pm 1, \pm 1)$  directions. Orange: electronlike Fermi surface ( $\partial A/\partial E > 0$ ) from the surface states. (c) Fermi surface of the hole-doped sample where four islands are connected and lead to a different cyclotron picture: blue: holelike; violet: electronlike; orange: electronlike.

due to the confinement. The valence band of the HgTe film reveals a deep minimum at the  $\Gamma$  point with four shallow side maxima along the  $(\pm 1, \pm 1)$  directions (see Fig. 1). The minimum is due to the mixing between light and heavy-hole states in the inverted band structure of HgTe [20,21].

## II. EXPERIMENT

### A. Technique

The magneto-optical experiments were carried out on a strained 80-nm-thick HgTe film grown by molecular beam epitaxy on a (100)-oriented GaAs substrate [18,22] with a lateral size of  $5 \times 5 \text{ mm}$ . The layer was sandwiched between the cap and the buffer layers of  $\text{Cd}_{0.7}\text{Hg}_{0.3}\text{Te}$  to obtain high electron mobility in the sample. The analysis of the cyclotron resonance corresponding to the upper surface state revealed the mobility to be up to  $\mu = e\tau/m_c = 5 \times 10^5 \text{ cm}^2 \text{ V}^{-1} \text{ s}^{-1}$ . Here,  $e$ ,  $\tau$ , and  $m_c$  are the electron charge, the scattering time, and the cyclotron mass, respectively. Between the layered structure and the GaAs substrate a  $5\text{-}\mu\text{m}$ -thick CdTe buffer layer was placed. To produce the semitransparent gate electrode, the film was covered on top by a multilayer insulator of  $\text{SiO}_2/\text{Si}_3\text{N}_4$  and a semitransparent metallic 10.5-nm-thick Ti-Au layer. The top-gate electrode allowed the variation of the Fermi energy to probe the surface states and the valence and conduction bands [6,23,24]. The shape of the gate electrode allowed a fully covered center of the sample for terahertz transmission measurements and four contacts at the corners of the sample, allowing to acquire simultaneous information about the electrical conductivity in the system.

Due to the fact that the gate only partially covers the sample, we were not able to fully rely on the magnetotransport measurements. The ungated regions can significantly falsify the transport response. However, at zero gate voltage, this ef-

fect is minimized, thus, allowing us to gather some additional information about the carriers in the system as shown below.

The cyclotron resonance was investigated in a Mach-Zehnder interferometer [25] arrangement, which allowed to measure the amplitude and the phase shift of the transmitted electromagnetic radiation with controlled polarization of light [23,26]. Continuous monochromatic radiation was produced by backward-wave oscillators operating in the submillimeter regime (100–1000 GHz). The transmitted radiation was detected by a silicon 4.2-K bolometer with a high-frequency cutoff filter of 3 THz. The data were obtained at several fixed frequencies in sweeping magnetic fields. Additional information about the charge carriers in the system was also obtained from the frequency-dependent spectra in a zero magnetic field. To unambiguously separate the resonances from the electronlike and holelike carriers, several experiments were conducted with circularly polarized radiation. The experiments were carried out at 1.8 K in a split-coil superconducting magnet that provided a magnetic field up to  $\pm 7 \text{ T}$  in the Faraday geometry; i.e., a magnetic field was applied parallel to the  $\mathbf{k}$  vector of the terahertz radiation.

### B. Spectra modeling

In order to obtain the parameters of the charge carriers, such as the two-dimensional (2D) density  $n$ , the effective cyclotron mass  $m_c$ , and the intrinsic scattering time  $\tau$ , the acquired experimental data were fitted using the Drude model for dynamical conductivity in the quasiclassical approximation [27]. We utilize the geometry with circularly polarized light and the conductivity written as

$$\sigma_+ = \frac{\sigma_0}{1 - i\tau(\omega + \Omega_c)}. \quad (3)$$

Here,  $\sigma_0 = ne^2\tau/m_c$  is the two-dimensional DC conductivity. The conductivity of a system with multiple carriers is the sum of the individual conductivities. Neglecting the influence of the substrate, the simplified expression for the transmission of circularly polarized radiation through a film (assumed to be thin compared to the radiation wavelength) can be written as

$$t_+ = 1 - \frac{i}{\tau_{\text{SR}}} \frac{1}{(\omega + i\Gamma) - \Omega_c}. \quad (4)$$

Here the “total” scattering rate  $\Gamma = 1/\tau + 1/\tau_{\text{SR}}$  describes the effective width of the cyclotron resonance observed in the transmission signal,  $1/\tau$  is the transport scattering rate,  $1/\tau_{\text{SR}} = ne^2 Z_0/2m_c$  is the superradiant damping [28], and  $Z_0$  is the impedance of the free space.

To take into account the reflections inside the substrate, we employed a more accurate model for the analysis of the experimental results. The procedure utilizes similar algebra as described previously [21,29,30]. The theoretical transmission of the circular polarization  $t_+ = t_{xx} + it_{xy}$  was calculated by changing into the basis with parallel  $t_{xx}$  and crossed  $t_{xy}$  transmission coefficients.

## III. THEORETICAL MODEL

To acquire a more detailed insight into the band structure of the strained HgTe layer, theoretical calculations have been performed using a multiband  $\mathbf{k}\cdot\mathbf{p}$  model [31] which takes into

account the strong coupling between the lowest conduction and the highest valence bands. The  $\mathbf{k} \cdot \mathbf{p}$  model considers eight bands: two  $\Gamma_6$ , two  $\Gamma_7$ , and four  $\Gamma_8$  subbands. Yet, considering the energy region of our interest, the contribution of the  $\Gamma_7$  subband is below 1%. The calculations were performed for a fully strained HgTe film with  $\text{Cd}_{0.7}\text{Hg}_{0.3}\text{Te}$  barriers which are grown on a CdTe substrate. The strain due to the lattice mismatch between HgTe and CdTe of about 0.3% leads to an opening of a direct gap of  $\approx 22$  meV (the indirect gap is about 10–15 meV) between the heavy-hole and light-hole bands in the HgTe layer [17]. We take the strain effects into consideration by applying a formalism introduced by Bir and Pikus [32]. According to the previous studies of similar structures [8,17,33], the crossing point of the surface states is located below the bulk band gap. Accordingly, a full-band envelope function approach [34] is used to perform the self-consistent calculations of the Hartree potential. This procedure avoids the separation of the occupied electron and hole states which is complicated for structures where both are occupied simultaneously. Our calculations include the structure inversion asymmetry and, therefore, effectively reproduce the experimental effect of the applied gate. The spatial distribution of charge can be calculated while the total charge density is being varied. The Hartree potential determined by this spatial distribution of charge (see Eq. (2) in Ref. [34]) splits the bulk and surface states and leads to their realignment, resulting in significant band-structure modifications (see Figs. 5 and 6 and the discussion below).

There is an ongoing debate in the literature about the influence of the interface inversion asymmetry (IIA) [35] on the band structure of HgTe structures. Several studies argue a sufficient effect of IIA in HgTe quantum wells grown on (013) substrates [36–38]. Moreover, theoretical calculations in Ref. [35] predict a gap of about 15 meV caused predominantly by IIA in (001) HgTe quantum wells of critical thicknesses. However, experimental data [15,39] do not confirm these predictions. Considering the complexity of the band structure of 80-nm HgTe layers and the missing experimental evidence of the influence of the IIA, we do not include these terms in our calculations.

In an attempt to test further anisotropy terms in the Hamiltonian, we tried to include the bulk inversion asymmetry (BIA) [40] term in calculation of the band structure at the charge neutrality point ( $n_{\text{tot}} = 0$ ). As demonstrated in Fig. S9 of the Supplemental Material in Ref. [41], the inclusion of this term strongly splits the valence bands and reduces the value of the gap. As the latter even worsens the agreement between theory and experiment (see Fig. 5 below), the BIA term was not used in the calculations of the band structure.

The plots of the surface band, the first valence band, and the first conduction band calculated using the  $\mathbf{k} \cdot \mathbf{p}$  model are shown in Fig. 1 for the case of the charge neutrality point: The densities of the holes and electrons are equal, and the total charge density equals  $n_{\text{tot}} = 0$ . Here, all three bands are spin degenerate. In this case, the Fermi energy crosses the surface, and the valence bands, thus, forming four islands in the valence band as shown in Fig. 1(b).

In the cyclotron signal, we expect an electronlike resonance due to the surface states and a holelike signal from the valence islands. After lowering the Fermi energy, the four regions of

the valence band connect forming a ring structure as shown in Fig. 1(c). In this case, the fourfold “valley” degeneracy is lifted, and each curve of the valence-band ring corresponds to a separate cyclotron resonance: a holelike signal from the outer curve (blue) and an electronlike signal from the inner curve (violet). The latter effect is due to a different sign of  $\partial A/\partial E$  in Eq. (1); positive curvature: electrons; negative curvature: holes. We note that, even in this case, a separate surface resonance is expected that remains electronlike. The island-ring transition is present even if we take into account that the band structure deforms with varying density and that all bands are spin polarized due to broken symmetry. After the Fermi surface is determined from the band-structure calculations, the theoretical cyclotron mass can be calculated using the definition in Eq. (1).

To obtain the density dependence of the cyclotron mass within the present theory, the effect of the applied gate was modeled by varying the total charge density in the system from  $6 \times 10^{11} \text{ cm}^{-2}$  (holes) to  $-6 \times 10^{11} \text{ cm}^{-2}$  (electrons) with the Fermi level reaching the valence and conduction subbands, respectively. For each value of the  $n_{\text{tot}}$ , the cyclotron mass was calculated using Eq. (1) as a function of density within the corresponding bands.

Finally, the theoretical band structure confirms the rotational symmetry of both surface states and bulk conduction subbands, thus justifying the use of Eq. (2) to connect the Fermi vector and the cyclotron mass. On the other hand, the hole islands do not show this isotropic behavior. Nevertheless, at lower hole concentration, the islands can be approximated as circles [see Fig. 1(b)] with an effective radius  $k_{\text{eff}}$  shifted by  $k_0 \approx (\pm 0.15, \pm 0.15) \text{ nm}^{-1}$  from the  $\Gamma$  point. In this case,  $k = k_{\text{eff}}$  in Eq. (2), where  $k_{\text{eff}}$  is related to the Fermi-surface area of each of the four islands as  $A = \pi k_{\text{eff}}^2$ . Of course, the exact relation between  $A$  and  $k_{\text{eff}}$  can be calculated from the theory. We believe, however, that a reasonable picture of the band structure can be obtained within an isotropic approximation as well. A direct comparison between theory and experiment can be performed using an approximation-independent plot of cyclotron masses vs density (see Fig. 4 below). This presentation is not sensitive to approximations performed in Eq. (2).

## IV. RESULTS AND DISCUSSION

### A. Cyclotron resonance

Figure 2 shows typical field-dependent transmission in the geometry with circularly polarized radiation. The advantage of this geometry is the clear separation of the electron (**e**) and hole (**h**) resonances as they are observed for positive and negative external magnetic fields, in agreement with Eq. (3). The inset in Fig. 2 demonstrates linear field dependence of the cyclotron resonance frequency ( $\omega = 2\pi\nu$ ), thus, verifying the application of the quasiclassical approximation in Eqs. (1) and (2). The data at low frequency (142 GHz) shown in Fig. 2(a) are most sensitive to the overall behavior of the charge carriers as, here, electrons and holes may be easily observed simultaneously, and they, indeed, can be well separated for the  $U_g = -10$ -V curve. For large negative voltages, the Fermi energy is situated in the valence band. The cyclotron signal from the holelike carriers can be observed in the gate voltage

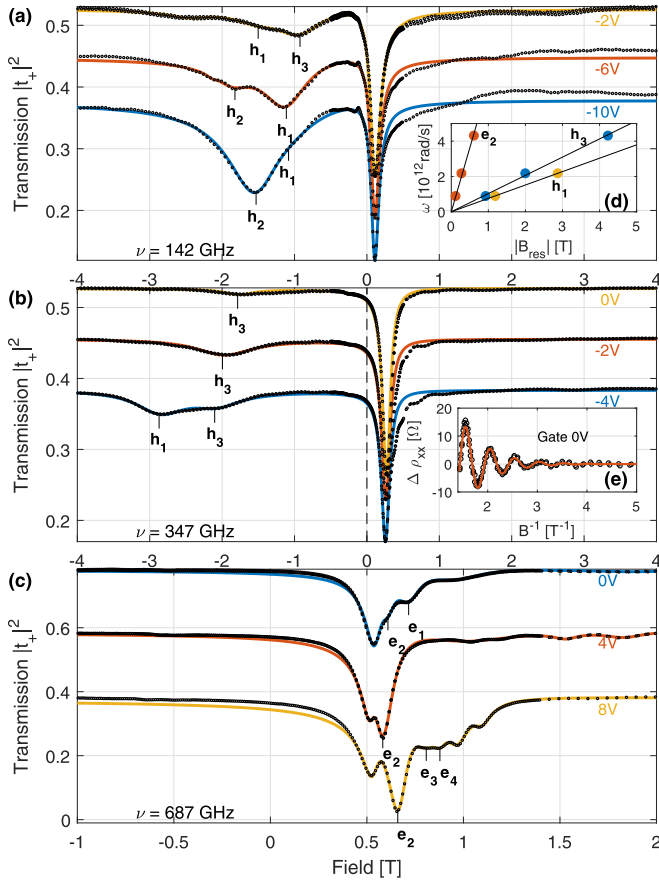


FIG. 2. Cyclotron resonance with circularly polarized light. (a)–(c) The intensity of the transmitted radiation  $|t_+|^2$  as a function of an external magnetic field for fixed frequencies as indicated. Resonance features for positive and negative fields correspond to electrons and holes, respectively. Points: experiment; solid lines: theoretical model based on Drude conductivity, Eq. (3). The absolute scales refer to the lowest curves, the others are shifted for clarity. The inset (d) shows the field dependence of the cyclotron resonance demonstrating linear behavior within the quasiclassical approximation according to Eqs. (1) and (2). (e) The oscillating part of the longitudinal resistivity at zero gate voltage. The experimental data (black circles) were fitted by a single-carrier Lifshits-Kosevich model (orange line).

range from  $-10$  to  $0$  V. This correlates with the position of the charge neutrality point that has been estimated from the resistivity measurements: The longitudinal resistivity  $\rho_{xx}$  showed a maximum at around  $-3$  V. With increasing gate voltage, the single resonance of the electrons reveals a distinct structure that is most clearly seen in the data at  $687$  GHz, Fig. 2(c).

The transmission curves can be fitted well using the procedure presented in Sec. II B (solid lines in Fig. 2). From the analysis of the resonances in the transmission, we obtain the 2D charge density, effective cyclotron mass, and the scattering time for each separate carrier type. A gradual increase in density with increasing gate voltage is expected for electrons. Similarly, the density of the holelike carriers must be a decreasing function of the gate voltage. Therefore, in the analysis of the band structure, only the resonances caused by carriers with monotonous gate-voltage dependence of the

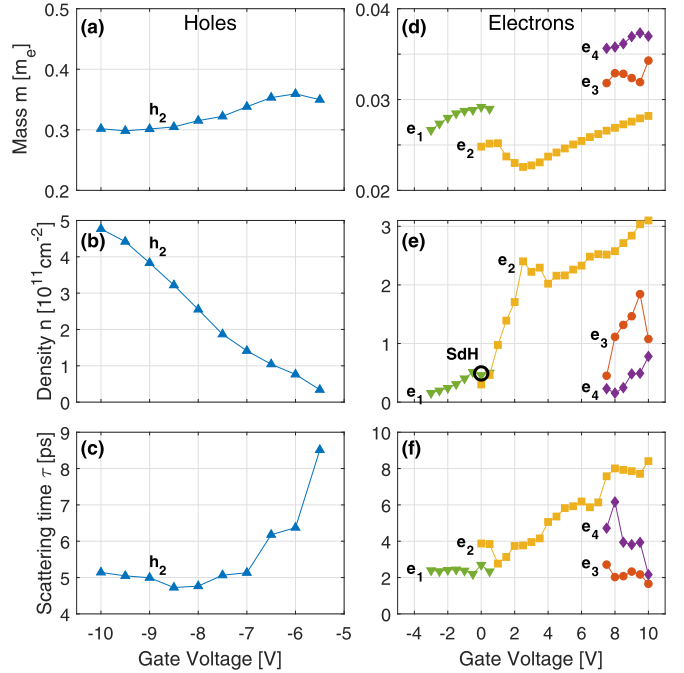


FIG. 3. Electrodynamical parameters of the cyclotron resonances in HgTe. (a)–(c) Holelike carriers, (d)–(f) electronlike carriers. Only the most relevant resonances which may be explained via a quasiclassical picture are shown. Colored symbols are experimental data from the fits of the spectra in Fig. 2. The black circle corresponds to the density  $\frac{n_{\text{SdH}}}{2}$  resulting from the Shubnikov–de Haas (SdH) analysis from Fig. 2(e). The lines are guides to the eye.

charge density were taken into account. For completeness, the electrodynamic parameters of the remaining resonances are given in the Supplemental Material in Ref. [41]. We believe that the majority of the additional peaks represents direct transitions between Landau levels and, thus, cannot be described via the quasiclassical approximation using Eqs. (1) and (2). For example, carriers  $h_1$  and  $h_3$  in Fig. 2 showed a nonmonotonous gate-voltage dependence of density and were, therefore, not considered in the band-structure analysis. Nevertheless, we were able to recognize them at multiple frequencies, showing a characteristic behavior of charged carriers in our model. Currently, the gate-voltage dependence of the intensity of these modes cannot be used to extract their density since their behavior goes beyond the quasiclassical approach.

Figure 3 shows the parameters of the cyclotron resonances that will be used to obtain the band structure of the 3D TI. The charge density decreases with the gate voltage for holes and increases for electrons. Both agree with the sign of the charge carriers obtained directly from the spectra in Fig. 2.

Additional information about the carriers in the sample was gathered by four-point longitudinal resistivity measurements at zero gate voltage, which displayed strong SdH oscillations as plotted against the reciprocal magnetic field in Fig. 2(e). The Lifshits-Kosevich formula [37,42,43] can be used to extract the carrier properties from the oscillation period. A model with a single carrier type fits the experimental data reasonably well [see the orange curve in Fig. 2(e)]. The oscillation frequency  $f$  can be transformed into the carrier density

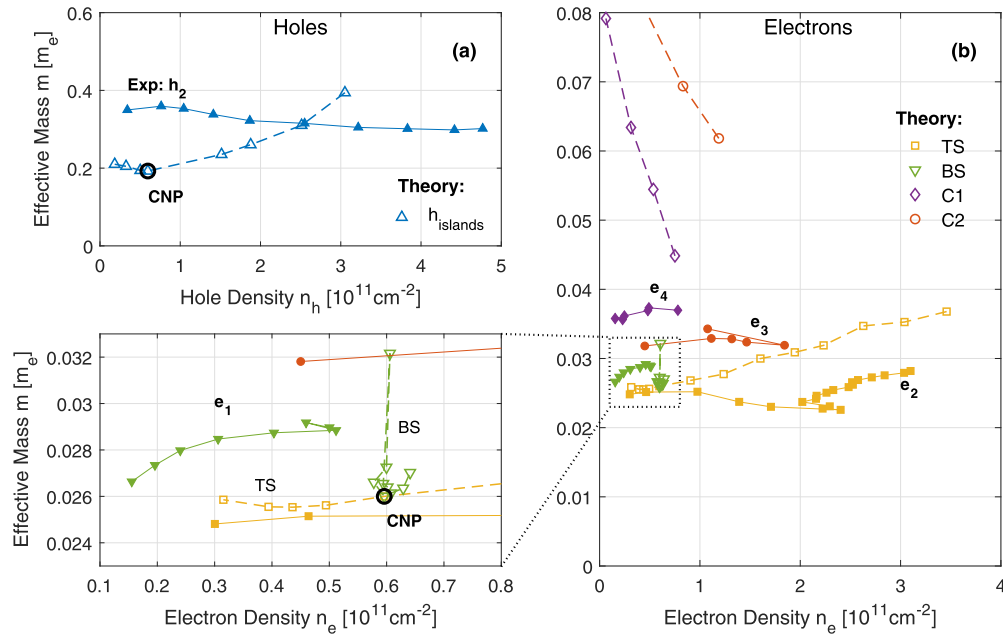


FIG. 4. Comparison of the cyclotron masses in strained HgTe with  $\mathbf{k} \cdot \mathbf{p}$  model calculations. Compared to Fig. 3, the cyclotron masses are plotted as a function of density. This presentation allows the comparison with the theoretical model without integrating Eq. (2). (a) Holelike carriers. (b) Electronlike carriers. Full symbols: experimental values; empty symbols: theory; BS: bottom surface states; TS: top surface states; C1, C2: spin-polarized bulk conduction bands; CNP: charge neutrality point.

by  $n = efD/h$ , where  $D$  represents the degeneracy of states. Assuming a double-degenerate state ( $D = 2$ ), we obtained  $n_{\text{SdH}} = 0.98 \times 10^{11} \text{ cm}^{-2}$ . As seen in Fig. 3(e),  $\frac{n_{\text{SdH}}}{2}$  overlaps with the densities of carriers  $\mathbf{e}_1$  and  $\mathbf{e}_2$ . As discussed below, these carriers can be attributed to bottom and top surface states, respectively. Note that SdH oscillations are mostly sensitive to the carriers density  $n$ . In the present case, the magnetotransport signal does not show any clear indication of the presence of two carrier types with different densities. In fact, Landau filling factors  $\nu = n_{\text{SdH}}/(B_{\text{min}}e/h)$  at the minima of  $\rho_{xx}$  seems to give odd values ( $\nu = 7, 9, 11, 13, 15$ ), which is a characteristic signature of a double-degenerate Dirac system [24,39,44].

To compare theory and experiment without using isotropic approximation, the cyclotron mass can be plotted directly as a function of the 2D density. This presentation is given in Fig. 4 where the  $\mathbf{k} \cdot \mathbf{p}$  predictions are shown with empty symbols and the experimental results with full symbols.

The theoretical points were obtained for a discrete number of  $n_{\text{tot}}$  as discussed in Sec. III. A scattering in the theoretical data comes from several effects: (i) numerical integration of area  $A$  in Eq. (1) with a discrete number of  $k$  points, (ii) from the anticrossings of the subbands, and (iii) from a finite value of the lateral lattice constant ( $a = 1 \text{ nm}$ ) in the full-band envelope-function approach used for the self-consistent calculations.

We note that the approximate density independence of the majority of the observed carriers in Figs. 4(a) and 4(b) suggests that the dispersion relations will have a parabolic-like shape. Indeed, inserting  $E = \hbar^2 k^2 / 2m_c$  into Eq. (2) gives the momentum and density-independent cyclotron mass  $m_c = eB/\Omega_c = \text{const}(n, k_F)$ . However, since hybridization of

multiple subbands takes place in the system, we do not expect a simple parabolic band structure, but one with higher-order corrections.

Comparing the experimental points [solid symbols in Fig. 4(a)] with theoretical predictions, we recognize the  $\mathbf{h}_2$  carriers as the fingerprint of the first spin-polarized valence band with four degenerate islands pockets in the band dispersion. Apparently, within the gate-voltage range of the present experiment, we did not reach the region of the ringlike Fermi surface nor the rest of the valence subbands at lower energies. Most likely, this is due to the flatness of the band structure at the transition point which leads to small values of  $\partial E_f / \partial U_g$ . Experiments in quantizing magnetic fields previously showed a transition line involving the hole Landau level in a 20-nm sample [45]. Nevertheless, our results exhibit the first detection of a hole carrier in a 3D TI by quasiclassical cyclotron resonance analysis.

Experimental values show fairly flat behavior of the hole mass vs its density, whereas the theoretical values are slightly increasing. The weak increase was as well experimentally and theoretically observed for much thinner samples ( $d \leq 20 \text{ nm}$ ) [37]. Currently, the reasons behind the mismatch between experiment and theory are not clear. Two factors can impact the experimental values here: (i) The experimental data for holes were obtained at high values of gate, which leads to deformation of the band structure, and (ii) due to relatively low hole density and high magnetic fields ( $\sim 1.5 \text{ T}$ ), we are approaching the limit where transitions between single Landau levels start to dominate.

Figure 4(b) shows the comparison of the cyclotron mass of the electronlike carriers with model calculations. We start with the analysis of the theoretical mass-density relations of

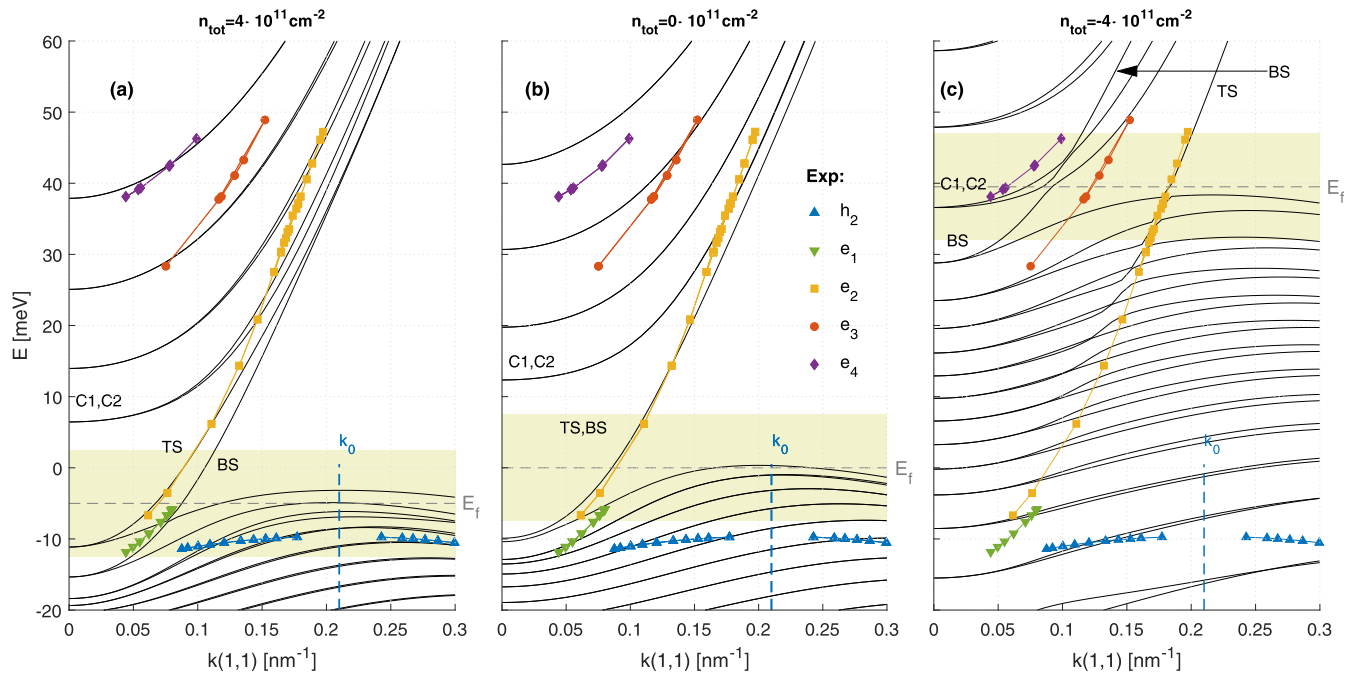


FIG. 5. Band structure of the three-dimensional topological insulator based on a strained HgTe along the (1,1) direction. Symbols: experimental data obtained from cyclotron mass; solid lines are predictions of the  $\mathbf{k} \cdot \mathbf{p}$  model for three values of the total charge density: (a) hole doping:  $n_{\text{tot}} = 4 \times 10^{11} \text{ cm}^{-2}$ , (b) charge neutrality:  $n_{\text{tot}} = 0$  and (c) electron doping:  $n_{\text{tot}} = -4 \times 10^{11} \text{ cm}^{-2}$ . Areas highlighted in yellow present the regions where it is valid to compare experimental results with theory.

the surface states that are marked by TS and BS. The density of the TS states (yellow open squares) can be changed by applying the gate voltage within the full range of Fig. 4(b). We observe approximate density independence of the cyclotron mass for the top surface states supporting the paraboliclike form of the surface band. We interpret the experimentally determined carriers  $\mathbf{e}_2$  (yellow full squares) as the top surface carriers as their parameters are close to the results of the theory.

On the contrary, the theoretical model predicts only weak variation of the electron density at the bottom surface as a function of doping [green open triangles, magnified part of Fig. 4(b)], which is due to screening of the potential by the top surface (see also Fig. 6). In the same mass range, we observe the carriers  $\mathbf{e}_1$  (green full triangles) that probably correspond to the electrons on the bottom surface. Looking back at Fig. 3(d), we observe that the carriers  $\mathbf{e}_3$  are possibly a continuation of  $\mathbf{e}_1$ . Therefore, we interpret  $\mathbf{e}_3$  as the bottom surface carriers as well. The gap between these two carriers in Fig. 3(d) might be the result of a dominating cyclotron signal by the top surface carriers  $\mathbf{e}_2$  at the gate voltages between +1 and +7 V.

The  $\mathbf{k} \cdot \mathbf{p}$  model predicts that the bottom of the bulk conduction band can be reached at high electron densities. For such high voltages, not only the top and bottom surfaces are strongly split, but also the spin degeneracy of the conduction band is lifted [see Fig. 5(c)]. Thus the theory predicts two cyclotron resonances from the bulk conduction band in the relevant doping range that are shown in Fig. 4(b) by open diamonds (C1) and open circles (C2). Comparing these predictions with the experiment, we suggest that carriers  $\mathbf{e}_4$  correspond to bulk conduction electrons C1.

Finally, we note that, within an alternative description, the electronlike signals  $\mathbf{e}_3$  and  $\mathbf{e}_4$  could be identified as C1 and C2 especially since they were observed simultaneously as soon as the Fermi level in the system reached the conduction bands. However, this interpretation provides a less convincing agreement between theory and experiment.

### B. Band structure of 3D TI

To access the experimental band structure of the HgTe film, the charge density of electrons is transferred to the electron momentum using the relation  $k = \sqrt{4\pi n/D}$  [15]. According to the identification of the carriers in the previous section, we

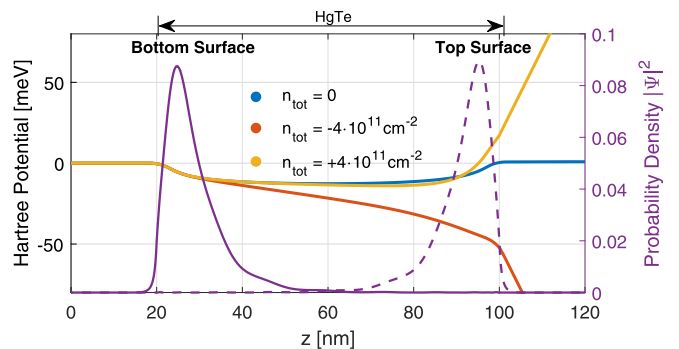


FIG. 6. Hartree potential and spatial distribution of the wave functions for the top and bottom surface states. Hartree potential (left axis) at neutral, electron, and hole dopings that is self-consistently determined as described in Sec. III. The spatial probability distribution (right axis) of the surface states at  $n_{\text{tot}} = 0$  is superimposed on the Hartree potential.

assume single degeneracy ( $D = 1$ ) for all electronlike carriers. We classified  $\mathbf{h}_2$  hole carriers as fourfold valley degenerate and spin-polarized hole-pocket states, thus, taking  $D = 4$ . According to the model calculations, the four local maxima of the valence band are expected at finite wave-vector  $k_0 \approx (\pm 0.15, \pm 0.15) \text{ nm}^{-1}$ . The maximum of the experimental valence band has been shifted by this value. As pointed out in Sec. III, for holelike carriers, we calculate the  $k$  vector along the (1,1) direction as  $k = k_0 \pm k_{\text{eff}}$  with  $k_{\text{eff}} = \sqrt{\pi n}$ .

The band dispersion, calculated within the approximation above, is shown in Fig. 5 as solid symbols. Direct integration lacks in providing the absolute energy position of the bands. Since we assume that the gate voltage defines a constant Fermi level in the film, the bands are vertically aligned to each other by referring to the gate voltage at which they were mutually detected.

In Fig. 5, we plot the theoretical band structure for three different doping ranges: (a) hole-doped regime with  $n_{\text{tot}} = +4 \times 10^{11} \text{ cm}^{-2}$ , (b) undoped regime with  $n_{\text{tot}} = 0$ , and (c) electron-doped regime with  $n_{\text{tot}} = -4 \times 10^{11} \text{ cm}^{-2}$ . The external electric field created by the applied gate drastically influences the energy spectrum as seen in Fig. 5. This variation of the band dispersion can be well understood taking into account the spatial distribution of the probability density of different states and the spatial dependence of the Hartree potential. These dependencies are shown in Fig. 6. Yellow, blue, and red curves show the Hartree potential for the same hole, neutral, and electron dopings as in Figs. 5(a)–5(c). The solid and dashed violet lines represent the probability distribution of the BS and TS states, respectively, at  $n_{\text{tot}} = 0$ . While varying  $n_{\text{tot}}$  does alter the distribution functions, the positions of the distribution maxima remain almost unchanged. Therefore, it is clearly evident that Hartree potential influences the top and bottom surfaces differently when  $n_{\text{tot}} \neq 0$ . It is well seen, that, at the position of the BS, the Hartree potential barely changes with  $n_{\text{tot}}$ , a consequence of the screening by all other carriers. This explains the weak gate dependence of the BS parameters in Fig. 4.

On the other hand, the TS experiences the strongest influence from the varying gate potential being easily split from the BS and shifted in energy in the band diagram. Latter is mostly evident at the positive gate voltages corresponding to electron doping with  $n_{\text{tot}} = -4 \times 10^{11} \text{ cm}^{-2}$ . The value of the Hartree potential at the position of the TS is around  $-40 \text{ meV}$ . This value directly corresponds to the shift of TS with respect to the  $E_f$ , when comparing the undoped and the electron-doped regimes presented in Figs. 5(b) and 5(c). Similar shifting occurs for the conduction and valence bands. However, the shifting amplitudes are smaller since the maxima of the corresponding wave functions lie in the bulk. The overlap between the bulk valence and TS wave functions leads to multiple crossings and anticrossings of their dispersion curves.

The variation of the gate voltage leads to shifting of the characteristic band energies and to the splitting of the bands that were degenerate at  $n_{\text{tot}} = 0$ . Therefore, the comparison between experiment and theory is valid in the vicinity of  $E_f$  only with  $E_f = E_f(n_{\text{tot}})$  being the Fermi level of the system. Three regions around Fermi energy corresponding to electron doping, hole doping, and the charge neutrality are shown by yellow shaded areas in Figs. 5(a)–5(c), and they are defined by

$E = E_f \pm 7.5 \text{ meV}$ . Also,  $U_g = 0 \text{ V}$  and the charge neutrality point do not coincide due to impurity doping—the experimental charge neutrality was found at  $U_g = -3 \text{ V}$ .

We start the discussion of the band structure with the region close to the charge neutrality point shown in panel (b). Here, according to theory, the bands are spin degenerate, and the size quantization of the valence and conduction bands is seen. As the Fermi energy lies in the vicinity of zero, the active states are expected to be the surface states and the valence-band holes. In the experiment, however, we have detected only the TS states. These states are marked as  $\mathbf{e}_2$  throughout this paper, and their dispersion fits well to the theoretical predictions without additional free parameters. On the other hand,  $\mathbf{e}_1$  and  $\mathbf{h}_2$  appeared at lower energies as the theory predicts.

In the hole-doped region, Fig. 5(a), we focus only on the data at lower energies. Here, both in the experiment and in the theory, we observe a clear splitting of the surface bands. These results are denoted as TS and BS in the model, and they correspond to  $\mathbf{e}_2$  and  $\mathbf{e}_1$  carriers, respectively. The reasons behind the vertical misalignment between the experimental and theoretical valence bands and the resulting increase of the indirect band gap remain unclear. Within our procedure, the energy position of the  $\mathbf{h}_2$  state cannot be shifted as it is fixed by the values of the gate voltage. Here, we would like to note that the inclusion of the BIA terms in our theoretical model resulted in an increase in the energy at which the valence holes appear and, therefore, an even greater mismatch with the experiment (see Fig. S9 of the Supplemental Material in Ref. [41]).

In the predominantly electronic doping regime shown in Fig. 5(c), the  $\mathbf{e}_2$  surface band nicely overlaps with the theoretical top surface band, which is subject to hybridization and crossings/anticrossings with several valence subbands. As discussed above, we attribute the carriers  $\mathbf{e}_3$  (solid red circles) to the bottom surface band and the carriers  $\mathbf{e}_4$  to one of the spin-polarized conduction bands (marked as C1).

Summarizing this section, in addition to two spatially separated surface bands in Fig. 5, the bulk valence, and conduction bands are accessed within the present experiment. Although the band structure is strongly influenced by the gate voltage, we observe reasonable coincidence between the  $\mathbf{k} \cdot \mathbf{p}$  model and the cyclotron resonance data. We recall that, in the theoretical model, all parameters are fixed by the known film structure and by the doping level of the layers.

## V. CONCLUSIONS

We investigated the cyclotron resonance of the three-dimensional topological insulator based on a HgTe film in the subterahertz frequency range. In addition to the resonances from the top and bottom surface states, separate modes are observed that correspond to bulk conduction and valence bands. The quasiclassical approach is utilized to analyze the parameters of the charge carriers, which is approved by the linearity of the cyclotron frequency in external magnetic fields. Within this approximation, the band structure can be extracted from the gate dependence of the magneto-optical spectra. Considering the obvious effect of the asymmetric gating potential on the sample, the experimental band structure agrees reasonably well with the predictions of the  $\mathbf{k} \cdot \mathbf{p}$  model. Especially for the case when the Fermi level is shifted to the valence band, clear deviations between theory and experiment are observed.

## ACKNOWLEDGMENTS

We acknowledge valuable discussions with S. Tarasenko. This work was supported by Austrian Science Funds (Grants No. W-1243, No. P27098-N27, and No. I3456-N27), by the

Russian Foundation for Basic Research (Grant No. 17-52-14007), and by the German Research Foundation Grants No. AS 327/5-1 and No. SFB 1143 (Project No. 247310070).

- 
- [1] A. Damascelli, Z. Hussain, and Z. X. Shen, Angle-resolved photoemission studies of the cuprate superconductors, *Rev. Mod. Phys.* **75**, 473 (2003).
- [2] K. S. Novoselov, A. K. Geim, S. V. Morozov, D. Jiang, M. I. Katsnelson, I. V. Grigorieva, S. V. Dubonos, and A. A. Firsov, Two-dimensional gas of massless Dirac fermions in graphene, *Nature (London)* **438**, 197 (2005).
- [3] Y. B. Zhang, Y. W. Tan, H. L. Stormer, and P. Kim, Experimental observation of the quantum Hall effect and Berry's phase in graphene, *Nature (London)* **438**, 201 (2005).
- [4] L. Zhang, Y. Zhang, J. Camacho, M. Khodas, and I. Zaliznyak, The experimental observation of quantum Hall effect of  $l=3$  chiral quasiparticles in trilayer graphene, *Nat. Phys.* **7**, 953 (2011).
- [5] G. M. Minkov, A. V. Germanenko, O. E. Rut, A. A. Sherstobitov, S. A. Dvoretzki, and N. N. Mikhailov, Hole transport and valence-band dispersion law in a HgTe quantum well with a normal energy spectrum, *Phys. Rev. B* **89**, 165311 (2014).
- [6] D. A. Kozlov, D. Bauer, J. Ziegler, R. Fischer, M. L. Savchenko, Z. D. Kvon, N. N. Mikhailov, S. A. Dvoretzki, and D. Weiss, Probing Quantum Capacitance in a 3D Topological Insulator, *Phys. Rev. Lett.* **116**, 166802 (2016).
- [7] D. A. Kozlov, M. L. Savchenko, J. Ziegler, Z. D. Kvon, N. N. Mikhailov, S. A. Dvoretzki, and D. Weiss, Capacitance spectroscopy of a system of gapless Dirac fermions in a HgTe quantum well, *JETP Lett.* **104**, 859 (2016).
- [8] J. N. Hancock, J. L. M. van Mechelen, A. B. Kuzmenko, D. van der Marel, C. Brüne, E. G. Novik, G. V. Astakhov, H. Buhmann, and L. W. Molenkamp, Surface State Charge Dynamics of a High-Mobility Three-Dimensional Topological Insulator, *Phys. Rev. Lett.* **107**, 136803 (2011).
- [9] M. Orlita, D. M. Basko, M. S. Zholudev, F. Teppe, W. Knap, V. I. Gavrilenko, N. N. Mikhailov, S. A. Dvoretzki, P. Neugebauer, C. Faugeras, A.-L. Barra, G. Martinez, and M. Potemski, Observation of three-dimensional massless Kane fermions in a zinc-blende crystal, *Nat. Phys.* **10**, 233 (2014).
- [10] C. Zoth, P. Olbrich, P. Vierling, K.-M. Dantscher, V. V. Bel'kov, M. A. Semina, M. M. Glazov, L. E. Golub, D. A. Kozlov, Z. D. Kvon, N. N. Mikhailov, S. A. Dvoretzki, and S. D. Ganichev, Quantum oscillations of photocurrents in HgTe quantum wells with Dirac and parabolic dispersions, *Phys. Rev. B* **90**, 205415 (2014).
- [11] K.-M. Dantscher, D. A. Kozlov, P. Olbrich, C. Zoth, P. Faltermeier, M. Lindner, G. V. Budkin, S. A. Tarasenko, V. V. Bel'kov, Z. D. Kvon, N. N. Mikhailov, S. A. Dvoretzki, D. Weiss, B. Jenichen, and S. D. Ganichev, Cyclotron-resonance-assisted photocurrents in surface states of a three-dimensional topological insulator based on a strained high-mobility HgTe film, *Phys. Rev. B* **92**, 165314 (2015).
- [12] A. Akrap, M. Haki, S. Tchoumakov, I. Crassee, J. Kuba, M. O. Goerbig, C. C. Homes, O. Caha, J. Novák, F. Teppe, W. Desrat, S. Koohpayeh, L. Wu, N. P. Armitage, A. Nateprov, E. Arushanov, Q. D. Gibson, R. J. Cava, D. van der Marel, B. A. Piot, C. Faugeras, G. Martinez, M. Potemski, and M. Orlita, Magneto-Optical Signature of Massless Kane Electrons in  $\text{Cd}_3\text{As}_2$ , *Phys. Rev. Lett.* **117**, 136401 (2016).
- [13] J. Chu and A. Sher, *Physics and Properties of Narrow Gap Semiconductors* (Springer, New York, 2007).
- [14] P. Yu and M. Cardona, *Fundamentals of Semiconductors: Physics and Materials Properties*, Advanced Texts in Physics Vol. 3 (Springer, Berlin, Heidelberg, 2005).
- [15] A. M. Shuvaev, V. Dziom, N. N. Mikhailov, Z. D. Kvon, Y. Shao, D. N. Basov, and A. Pimenov, Band structure of a two-dimensional Dirac semimetal from cyclotron resonance, *Phys. Rev. B* **96**, 155434 (2017).
- [16] N. W. Ashcroft and N. D. Mermin, *Solid State Physics*, HRW International Editions (Holt, Rinehart, and Winston, New York, 1976).
- [17] C. Brüne, C. X. Liu, E. G. Novik, E. M. Hankiewicz, H. Buhmann, Y. L. Chen, X. L. Qi, Z. X. Shen, S. C. Zhang, and L. W. Molenkamp, Quantum Hall Effect from the Topological Surface States of Strained Bulk HgTe, *Phys. Rev. Lett.* **106**, 126803 (2011).
- [18] D. A. Kozlov, Z. D. Kvon, E. B. Olshanetsky, N. N. Mikhailov, S. A. Dvoretzki, and D. Weiss, Transport Properties of a 3D Topological Insulator Based on a Strained High-mobility HgTe Film, *Phys. Rev. Lett.* **112**, 196801 (2014).
- [19] L. Fu and C. L. Kane, Topological insulators with inversion symmetry, *Phys. Rev. B* **76**, 045302 (2007).
- [20] K. Ortner, X. C. Zhang, A. Pfeuffer-Jeschke, C. R. Becker, G. Landwehr, and L. W. Molenkamp, Valence band structure of HgTe/Hg<sub>1-x</sub>Cd<sub>x</sub>Te single quantum wells, *Phys. Rev. B* **66**, 075322 (2002).
- [21] V. Dziom, A. Shuvaev, A. Pimenov, G. V. Astakhov, C. Ames, K. Bendias, J. Böttcher, G. Tkachov, E. M. Hankiewicz, C. Brüne, H. Buhmann, and L. W. Molenkamp, Observation of the universal magnetoelectric effect in a 3D topological insulator, *Nat. Commun.* **8**, 15197 (2017).
- [22] Z. D. Kvon, E. B. Olshanetsky, N. N. Mikhailov, and D. A. Kozlov, Two-dimensional electron systems in HgTe quantum wells, *Low Temp. Phys.* **35**, 6 (2009).
- [23] A. Shuvaev, A. Pimenov, G. V. Astakhov, M. Muhlbauer, C. Brüne, H. Buhmann, and L. W. Molenkamp, Room temperature electrically tunable terahertz Faraday effect, *Appl. Phys. Lett.* **102**, 241902 (2013).
- [24] C. Brüne, C. Thienel, M. Stuiber, J. Böttcher, H. Buhmann, E. G. Novik, C.-X. Liu, E. M. Hankiewicz, and L. W. Molenkamp, Dirac-Screening Stabilized Surface-State Transport in a Topological Insulator, *Phys. Rev. X* **4**, 041045 (2014).
- [25] A. A. Volkov, Y. G. Goncharov, G. V. Kozlov, S. P. Lebedev, and A. M. Prokhorov, Dielectric measurements in the submillimeter wavelength region, *Infrared Phys.* **25**, 369 (1985).
- [26] A. M. Shuvaev, G. V. Astakhov, C. Brüne, H. Buhmann, L. W. Molenkamp, and A. Pimenov, Terahertz magneto-optical

- spectroscopy in HgTe thin films, *Semicond. Sci. Technol.* **27**, 124004 (2012).
- [27] E. D. Palik and J. K. Furdyna, Infrared and microwave magnetoplasma effects in semiconductors, *Rep. Prog. Phys.* **33**, 1193 (1970).
- [28] J. Gospodarič, V. Dziom, A. Shuvaev, A. A. Dobretsova, N. N. Mikhailov, Z. D. Kvon, and A. Pimenov, Superradiant and transport lifetimes of the cyclotron resonance in the topological insulator HgTe, *Phys. Rev. B* **99**, 115130 (2019).
- [29] A. M. Shuvaev, G. V. Astakhov, A. Pimenov, C. Brüne, H. Buhmann, and L. W. Molenkamp, Giant Magneto-Optical Faraday Effect in HgTe thin Films in the Terahertz Spectral Range, *Phys. Rev. Lett.* **106**, 107404 (2011).
- [30] S. Candussio, G. V. Budkin, M. Otteneder, D. A. Kozlov, I. A. Dmitriev, V. V. Bel'kov, Z. D. Kvon, N. N. Mikhailov, S. A. Dvoretzky, and S. D. Ganichev, Cyclotron-resonance-induced photogalvanic effect in surface states of 200-nm-thick strained hgte films, *Phys. Rev. Mater.* **3**, 054205 (2019).
- [31] E. G. Novik, A. Pfeuffer-Jeschke, T. Jungwirth, V. Latussek, C. R. Becker, G. Landwehr, H. Buhmann, and L. W. Molenkamp, Band structure of semimagnetic  $\text{Hg}_{1-y}\text{Mn}_y\text{Te}$  quantum wells, *Phys. Rev. B* **72**, 035321 (2005).
- [32] G. L. Bir and G. E. Pikus, *Symmetry and Strain-Induced Effects in Semiconductors* (Wiley, Chichester, UK, 1974).
- [33] S.-C. Wu, B. Yan, and C. Felser, Ab initio study of topological surface states of strained HgTe, *Europhys. Lett.* **107**, 57006 (2014).
- [34] T. Andlauer and P. Vogl, Full-band envelope-function approach for type-II broken-gap superlattices, *Phys. Rev. B* **80**, 035304 (2009).
- [35] S. A. Tarasenko, M. V. Durnev, M. O. Nestoklon, E. L. Ivchenko, Jun-Wei Luo, and A. Zunger, Split Dirac cones in HgTe/CdTe quantum wells due to symmetry-enforced level anticrossing at interfaces, *Phys. Rev. B* **91**, 081302(R) (2015).
- [36] G. M. Minkov, A. V. Germanenko, O. E. Rut, A. A. Sherstobitov, M. O. Nestoklon, S. A. Dvoretzki, and N. N. Mikhailov, Spin-orbit splitting of valence and conduction bands in HgTe quantum wells near the Dirac point, *Phys. Rev. B* **93**, 155304 (2016).
- [37] G. M. Minkov, V. Ya. Aleshkin, O. E. Rut, A. A. Sherstobitov, A. V. Germanenko, S. A. Dvoretzki, and N. N. Mikhailov, Valence band energy spectrum of HgTe quantum wells with an inverted band structure, *Phys. Rev. B* **96**, 035310 (2017).
- [38] L. S. Bovkun, A. V. Ikonnikov, V. Y. Aleshkin, K. E. Spirin, V. I. Gavrilenko, N. N. Mikhailov, S. A. Dvoretzki, F. Teppe, B. A. Piot, M. Potemski, and M. Orlita, Landau level spectroscopy of valence bands in HgTe quantum wells: Effects of symmetry lowering, *J. Phys.: Condens. Matter* **31**, 145501 (2019).
- [39] B. Büttner, C. X. Liu, G. Tkachov, E. G. Novik, C. Brüne, H. Buhmann, E. M. Hankiewicz, P. Recher, B. Trauzettel, S. C. Zhang, and L. W. Molenkamp, Single valley Dirac fermions in zero-gap HgTe quantum wells, *Nat. Phys.* **7**, 418 (2011).
- [40] G. Dresselhaus, Spin-orbit coupling effects in zinc blende structures, *Phys. Rev.* **100**, 580 (1955).
- [41] See Supplemental Material at <https://link.aps.org/supplemental/10.1103/PhysRevB.102.115113> for additional experimental data and results from the bulk inversion asymmetry calculations.
- [42] E. M. Lifshits and A. M. Kosevich, Theory of the Shubnikov-de Haas effect, *J. Phys. Chem. Solids* **4**, 1 (1958).
- [43] A. A. Dobretsova, Z. D. Kvon, S. S. Krishtopenko, N. N. Mikhailov, and S. A. Dvoretzky, Spin splitting of surface states in HgTe quantum wells, *Low Temp. Phys.* **45**, 159 (2019).
- [44] A. H. Castro Neto, F. Guinea, N. M. R. Peres, K. S. Novoselov, and A. K. Geim, The electronic properties of graphene, *Rev. Mod. Phys.* **81**, 109 (2009).
- [45] M. Zholudev, F. Teppe, M. Orlita, C. Consejo, J. Torres, N. Dyakonova, M. Czapkiewicz, J. Wróbel, G. Grabecki, N. Mikhailov, S. Dvoretzki, A. Ikonnikov, K. Spirin, V. Aleshkin, V. Gavrilenko, and W. Knap, Magnetospectroscopy of two-dimensional HgTe-based topological insulators around the critical thickness, *Phys. Rev. B* **86**, 205420 (2012).